

Controlled morphogenesis and self-assembly of bismutite nanocrystals into three-dimensional nanostructures and their applications†

Cite this: *J. Mater. Chem. A*, 2014, 2, 2275

Xinyi Zhang,^{*ab} Yuanhui Zheng,^c Dougal G. McCulloch,^d Leslie. Y. Yeo,^{de} James. R. Friend^{be} and Douglas R. MacFarlane^{*a}

We report the morphogenesis and self-assembly of bismutite nanocrystals with fully tunable morphologies from square plates, octagonal sheets, and round disks into three-dimensional hierarchical nanostructures. The results show that the nucleation, growth and self-assembly of bismutite nanocrystals strongly depend on the synergistic effect between hydroxide and citrate ions. The three-dimensional hierarchical nanostructures are formed through an oriented-attachment of bismutite nanocrystals along the $\langle 001 \rangle$ directions. The bismutite hierarchical nanostructures can be utilized for efficient and selective adsorption and separation. A novel surface-enhanced Raman spectroscopy platform based on a bismutite/gold nanoparticles core-shell structure has been developed for ultrasensitive detection of aromatic molecules with a detection limit down to 1 nM.

Received 8th November 2013
Accepted 17th December 2013

DOI: 10.1039/c3ta14587e

www.rsc.org/MaterialsA

Introduction

The morphology of crystals is not only a field of pure scientific curiosity but also of significant interest in many fields of science and industry.^{1–3} Understanding the relationship between crystal morphology and atomic structure allows the prediction of crystal shape, the optimization of crystal growth, and the upgrade of the characteristics of materials. Controlled morphogenesis is currently of considerable interest in developing functional nanomaterials.^{4,5} In particular, the surface stability and activity of nanocrystals are largely dominated by their surface chemistry, whose effect on the equilibrium morphology is critical for the synthesis of nanomaterials with high reactivity and sensitivity.^{6,7} To date, many studies have investigated the morphogenesis of nanocrystals including noble metals such as Ag, Pd,^{8–10} and binary semiconductors such as zinc oxide, and cuprous oxide.^{11–14} However, only a few reports are available as yet of the synthesis of ternary nanocrystals with tunable morphology.^{15,16} In order to systematically study the relationship between synthesis, morphology, and

properties and explore their practical applications, the controlled morphogenesis of ternary nanocrystals and their complex nanostructures is highly desirable.¹⁷

Inspired by biomineralization processes, self-assembly of nanocrystals into complex or three-dimensional (3D) nanostructures has received much attention particularly for applications in energy and biomedical fields.^{18,19} The ability to produce various nanocrystals through simple synthetic strategies has opened up the possibility of assembling them into tailored superstructures. Our interest in designing functional nanostructures has inspired us to explore the possibility of self-assembling ternary nanocrystals with controlled morphologies into 3D hierarchical nanostructures and thereby their associated properties. Ternary bismutite ((BiO)₂CO₃, BSC) has long been used for medicinal purposes, as an anti-inflammatory, antibacterial, and antacid.^{20,21} Further, there is considerable interest in BSC nanomaterials given their utility in photocatalytic applications.^{22–26} Here, we present a facile approach for the fabrication and architecture of BSC nanocrystals with fully tunable morphologies from square plates, octagonal sheets and round disks into 3D hierarchical nanostructures. We find that the nucleation, growth and self-assembly of BSC nanocrystals strongly depend on a synergistic effect between hydroxide and citrate ions. Selective adsorption of citrate ions on BSC nanocrystals plays an important role in the morphology control of BSC nanocrystals and architecture of the 3D nanostructures. The 3D BSC hierarchical nanostructures can be utilized for efficient selective adsorption and separation. Finally, we demonstrate that the 3D BSC/Au nanoparticle core-shell spheres can act as an ultra-sensitive surface-enhanced Raman scattering (SERS) sensor.

^aSchool of Chemistry, Monash University, Clayton, VIC 3800, Australia. E-mail: xinyi.zhang@monash.edu; douglas.macfarlane@monash.edu; Fax: +61-399054597; Tel: +61-399024619

^bMelbourne Centre for Nanofabrication, Clayton, VIC 3800, Australia

^cSchool of Chemistry, The University of New South Wales, Sydney, NSW 2052, Australia

^dSchool of Applied Science, RMIT University, Melbourne, VIC 3000, Australia

^eMicro/Nanophysics Research Laboratory, RMIT University, Melbourne, VIC 3000, Australia

† Electronic supplementary information (ESI) available. See DOI: 10.1039/c3ta14587e

Experimental

Synthesis and characterization

BSC crystals were prepared *via* hydrothermal reaction of bismuth nitrate, and urea. In a typical synthesis of BSC square nanoplates, 30 ml solutions containing 10 mmol of bismuth nitrate ($\text{Bi}(\text{NO}_3)_3$) and 2.5 g urea were loaded into a Teflon autoclave after 30 min magnetic stirring. The NaOH concentration was adjusted to 0.1 M. The components of the solution for the synthesis of BSC octagonal sheets, round disks and hierarchical nanostructures are the same as above except for the addition of sodium citrate ($\text{Na}_3\text{C}_6\text{H}_5\text{O}_7$) and the change in the NaOH concentrations. The autoclave was sealed and maintained at 180 °C for 6 h and then allowed to cool naturally to room temperature. After rinsing with distilled water and absolute ethanol to remove possible residues, the products were finally dried at 60 °C and collected. All chemical reagents were of analytical grade and used without further purification. The 3D BSC/Au nanoparticles core-shell spheres were fabricated by using the 3D BSC nanostructures prepared at 40 mmol $\text{Na}_3\text{C}_6\text{H}_5\text{O}_7$ and 0.01 M NaOH. The BSC samples were activated in a solution containing 1 g per liter PdCl_2 and 5 g per liter HCl for 2 h, and then 5 mg of BSC samples were added to 2 ml of the following deposition solution: 12 g per liter HAuCl_4 , 10 g per liter $\text{N}_2\text{H}_4 \cdot \text{H}_2\text{O}$, 160 g per liter Na_2SO_3 , 5 g per liter EDTA, 30 g per liter K_2HPO_4 , 0.5 g per liter CoSO_4 ; PH 9.0. The growth and deposition of Au nanoparticles on the 3D BSC samples was carried out with a magnetic agitation at 60 °C for 4 h. The structure and morphology of the BSC crystals were investigated using an X-ray diffractometer (XRD, PW1140/90) with Cu $K\alpha$ radiation (25 mA and 40 kV), a scanning electron microscope (SEM, JEOL JSM-7001F), a transmission electron microscope (TEM, Philips CM20) and a high-resolution transmission electron microscope (HRTEM, JEOL-2011). Both TEMs were operated at 200 kV.

Adsorption and separation

The adsorption and separation applications of 3D BSC nanostructures were investigated by using rhodamine B (RhB) and methyl orange (MO). For the adsorption experiment, 10 mg of BSC samples prepared at 40 mmol $\text{Na}_3\text{C}_6\text{H}_5\text{O}_7$ and 0.01 M NaOH were added to 3 ml of 10 mg L^{-1} RhB solutions at pH 4, 7, and 11 under agitation. The pH of the solutions was adjusted by using 0.1 M HCl or 0.1 M NaOH. The concentrations of RhB were recorded according to the change of the absorbency of the dye solution. For the separation experiment, dyes were mixed at concentrations of 10 mg L^{-1} of RhB and 20 mg L^{-1} of MO, and the pH of the solutions was adjusted to 4. 10 mg of BSC samples were added into 3 ml of RhB and MO mixture solutions with agitation. The MO solution was removed through filtration after 2 h. The remaining BSC samples were subsequently rinsed with distilled water at pH 4. Finally, the BSC samples were added into 3 ml of distilled water at pH 11 to release the RhB. The absorbance of the dye solutions was recorded using an agilent Cary 60 ultraviolet-visible spectrometer. The zeta potential was measured using a zeta potential analyzer (Malvern, Zetasizer Nano-ZS).

Raman spectroscopy measurement

The obtained BSC/Au nanoparticles core-shell sphere sample was subsequently rinsed with distilled water. Then, the samples were exposed to UV-ozone at an oxygen flow rate of 3 L min^{-1} for 10 min. After the UV-ozone treatment, the samples were immersed in 2 ml of different concentrations of benzenethiol in ethanol solution and left for 12 h, upon which the samples were rinsed with ethanol and then dried. For comparison, a commercial Klarite SERS substrate was exposed to UV ozone and benzenethiol under the same conditions as the BSC/Au nanoparticles core-shell sphere samples prior to the SERS measurements. The Raman spectra were recorded using a Confocal micro-Raman System (Renishaw RM 2000) equipped with a near-IR diode laser at a wavelength of 782 nm (laser power: 1.15 mW and laser spot size: 1 μm). All of the Raman spectra were collected by fine-focusing a 50 \times microscope was 10 s.

Results and discussion

The morphologies of the BSC crystals obtained under various conditions were observed by scanning electron microscopy (SEM). In general, BSC crystals with shapes from square plates and octagonal sheets, to round disks were synthesized. The size of the BSC crystals depends on the NaOH concentration, increasing from hundreds of nanometers to tens of micrometers when the NaOH concentration was increased from 0.1 M to 3 M (Fig. 1). BSC square nanoplates with edge lengths of 300–600 nm and thicknesses of 20–50 nm were obtained at

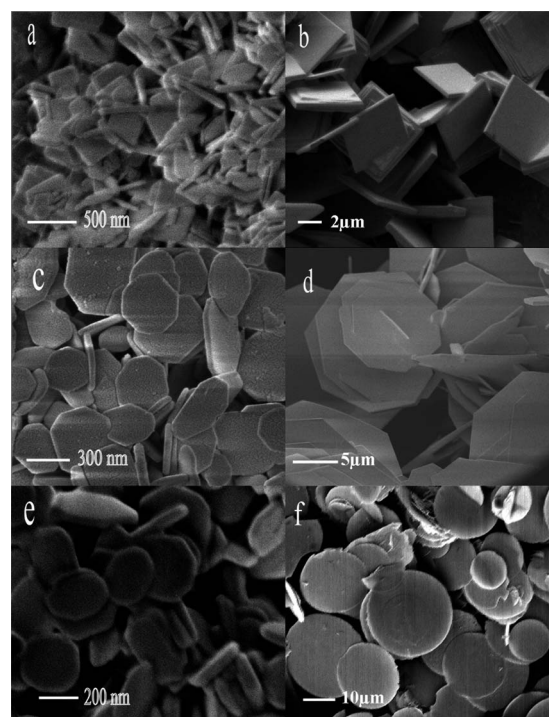


Fig. 1 SEM images of the BSC crystals obtained under different conditions: (a) 0.1 M NaOH. (b) 1 M NaOH. (c) 20 mmol $\text{Na}_3\text{C}_6\text{H}_5\text{O}_7$, 0.1 M NaOH. (d) 20 mmol $\text{Na}_3\text{C}_6\text{H}_5\text{O}_7$, 2 M NaOH. (e) 30 mmol $\text{Na}_3\text{C}_6\text{H}_5\text{O}_7$, 0.1 M NaOH. (f) 30 mmol $\text{Na}_3\text{C}_6\text{H}_5\text{O}_7$, 3 M NaOH.

0.1 M NaOH (Fig. 1a). BSC microplates with edge lengths of 5–6 μm and thicknesses of about 300 nm were obtained at 1 M NaOH (Fig. 1b). BSC octagonal nanosheets with edge lengths of 150–400 nm and thicknesses of 30–60 nm were obtained at 0.1 M NaOH in the presence of 20 mmol $\text{Na}_3\text{C}_6\text{H}_5\text{O}_7$, while octagonal microsheets with edge lengths of 5–10 μm and thicknesses of about 200 nm were obtained at 2 M NaOH in the presence of 20 mmol $\text{Na}_3\text{C}_6\text{H}_5\text{O}_7$ (Fig. 1c and d). With a further increase of $\text{Na}_3\text{C}_6\text{H}_5\text{O}_7$ concentration to 30 mmol, 100–250 nm nanodisks of 20–50 nm thickness were obtained at 0.1 M NaOH, increasing to 5–30 μm diameter and 200 nm thickness at 3 M NaOH (Fig. 1e and f). The very flat facets, sharp edges, and the good symmetry of the BSC crystals indicate that the structures have practically reached local equilibrium. The X-ray diffraction (XRD) patterns of the BSC crystals are shown in Fig. 2. All of the diffraction peaks can be indexed as the tetragonal structure of bulk BSC. It can be seen that the relative intensity of the peaks strongly depends on both NaOH and $\text{Na}_3\text{C}_6\text{H}_5\text{O}_7$ concentrations. In the conventional BSC samples, the relative intensity of the (013) reflection is the highest.²⁷ Here, most of the relative intensity of reflection of the (013) peak were much lower than the conventional values, and most of the predominant peaks result from the (002) reflections, suggesting that the materials have an abundance of (001) facets. Fig. 3a shows the TEM image of a BSC square nanoplate with a side length of about 600 nm. Its selected-area electron diffraction (SAED) pattern can be indexed as the (001) zone of bulk BSC with the expected (110) and (1 $\bar{1}$ 0) reflections (inset, Fig. 3a). The truncated edge of the BSC plate is enclosed by {100} facets, which are the main facets of the octagonal shaped BSC sheets that will be discussed further subsequently. High-resolution TEM image of regions indicated in Fig. 3a are displayed in Fig. 3b, in which clear (110) and (1 $\bar{1}$ 0) lattice fringes with respective spacings of 2.7 Å are visible. Fig. 3c shows a TEM image of the edge of a BSC octagonal nanosheet with an edge size of approximately 180 nm and the corresponding SAED pattern. The HRTEM image is displayed as Fig. 3d, exhibiting a (001) facet with one of the edges parallel to the {110} or {100} facets. Fig. 3e shows a TEM image

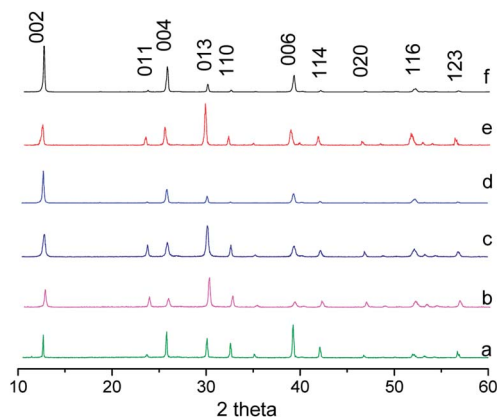


Fig. 2 XRD patterns of the BSC crystals synthesized under various conditions: (a) 0.1 M NaOH. (b) 1 M NaOH. (c) 20 mmol $\text{Na}_3\text{C}_6\text{H}_5\text{O}_7$, 0.1 M NaOH. (d) 20 mmol $\text{Na}_3\text{C}_6\text{H}_5\text{O}_7$, 2 M NaOH. (e) 30 mmol $\text{Na}_3\text{C}_6\text{H}_5\text{O}_7$, 0.1 M NaOH. (f) 30 mmol $\text{Na}_3\text{C}_6\text{H}_5\text{O}_7$, 3 M NaOH.

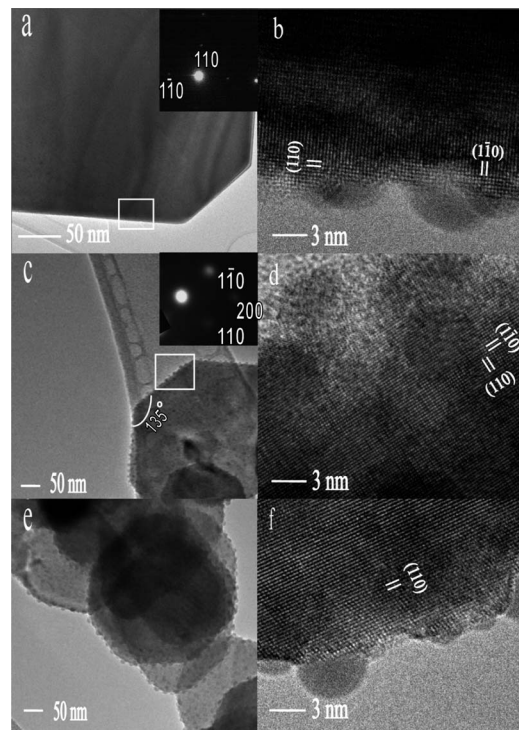


Fig. 3 (a) TEM image of a BSC square nanoplate and its corresponding electron diffraction pattern. (b) HRTEM image of the nanoplate. (c) TEM image of a BSC octagonal nanosheet and its corresponding electron diffraction pattern. (d) HRTEM image of the nanosheet. (e) TEM image of BSC round nanodisks. (f) HRTEM image of a nanodisk.

of the BSC nanodisks with a diameter of 300–400 nm. The corresponding HRTEM images are displayed in Fig. 3f. The BSC nanocrystals, especially in the case of BSC nanodisks, are very sensitive to the electron beam. After irradiation for 10 s under the electron beam at 200 kV, tiny particles with size about 2 nm emerged on the surface of the nanodisks, which could be attributed to the thermal decarboxylation of the BSC nanocrystals in high vacuum.²⁸

Three-dimensional BSC nanostructures with controlled crystalline morphology, orientation and surface architectures were fabricated through the self-assembly of BSC nanocrystals. Fig. 4 shows the SEM images of the 3D BSC nanostructures formed through assembly of various BSC nanocrystals. Fig. 4a and b show 3D BSC nanostructures prepared in the presence of 20 mmol sodium citrate and 0.01 M NaOH. The sphere-like 3D BSC nanostructures are composed of packed square nanoplates with 200–400 nm long edges and 30–40 nm thicknesses. Fig. 4c and d show the 3D BSC nanostructures prepared in the presence of 30 mmol sodium citrate and 0.01 M NaOH. The open-hole BSC nanostructures are composed of packed round nanosheets with 400–800 nm sizes and 40–60 nm thicknesses. Fig. 4e and f show the 3D BSC nanostructures prepared in the presence of 40 mmol sodium citrate and 0.01 M NaOH. The 3D BSC nanostructures are composed of close packed nanodisks with diameters of 100–500 nm and thicknesses of 20–40 nm, respectively. The X-ray diffraction patterns of the 3D BSC nanostructures are shown in Fig. 5. In comparison with BSC

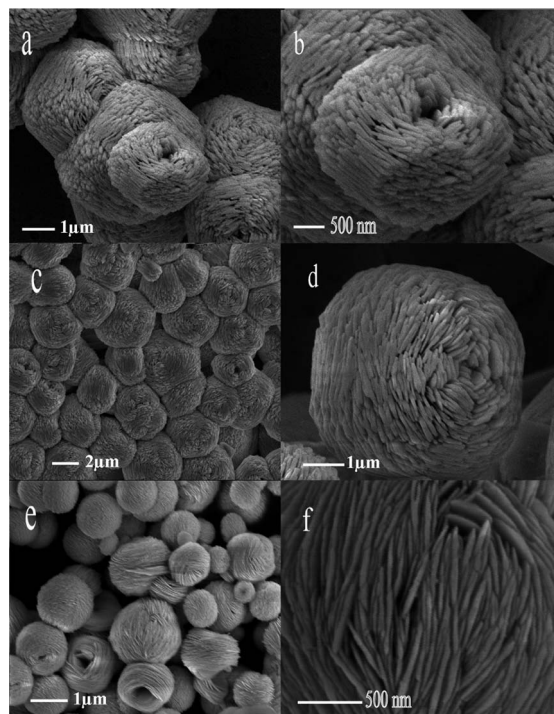


Fig. 4 SEM images of the 3D BSC nanostructures obtained under different conditions: (a and b) 20 mmol $\text{Na}_3\text{C}_6\text{H}_5\text{O}_7$, 0.01 M NaOH. (c and d) 30 mmol $\text{Na}_3\text{C}_6\text{H}_5\text{O}_7$, 0.01 M NaOH. (e and f) 40 mmol $\text{Na}_3\text{C}_6\text{H}_5\text{O}_7$, 0.01 M NaOH.

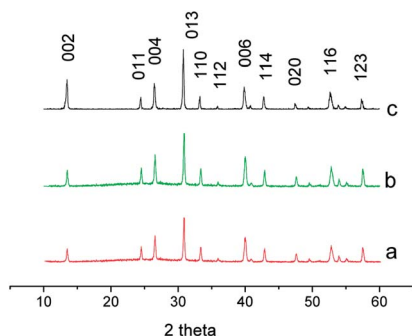


Fig. 5 XRD patterns of the BSC nanostructures obtained under different conditions: (a) 20 mmol $\text{Na}_3\text{C}_6\text{H}_5\text{O}_7$, 0.01 M NaOH. (b) 30 mmol $\text{Na}_3\text{C}_6\text{H}_5\text{O}_7$, 0.01 M NaOH. (c) 40 mmol $\text{Na}_3\text{C}_6\text{H}_5\text{O}_7$, 0.01 M NaOH.

nano- and microcrystals, the $\{001\}$ peaks are less pronounced because fewer $\{001\}$ facets are exposed due to the stacking and angles. Fig. 6a and b show TEM images of the plain and cross-section views of the 3D BSC nanostructures prepared in the presence of 40 mmol sodium citrate and 0.01 M NaOH, respectively. The inset in Fig. 6a shows the corresponding SAED pattern. The 3D BSC nanostructures exhibit open-hole hollow structures composed of stacked nanosheets with 10–30 nm thicknesses (see also Fig. S1 in the ESI†). The HRTEM images of the cross-section and plane views of the nanosheets confirm that the $\{001\}$ is the main facet of these nanoplates (Fig. 6c and d). Based on the observation by both TEM and SEM, it can be

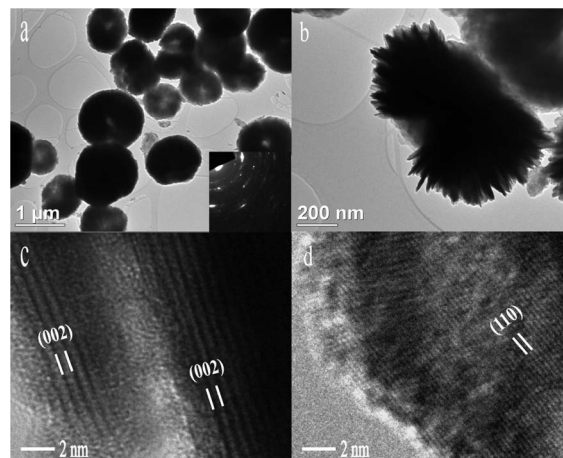


Fig. 6 (a and b) TEM images and (c and d) HRTEM images of the 3D BSC nanostructures prepared with 40 mmol $\text{Na}_3\text{C}_6\text{H}_5\text{O}_7$, 0.01 M NaOH.

concluded that the 3D BSC nanostructure are composed of nanosheets with their broad surface stacking along the $\langle 001 \rangle$ directions.

Understanding the mechanism by which these structures are formed is important in crystal growth, where a large quantity of crystals with well controlled sizes and morphologies are required. However, the nucleation and crystallization of BSC crystals at the microscopic scale has yet to be reported. Here, the morphologies of the BSC crystals should shed light on the mechanism by which they are formed. As illustrated in a previous study, BSC is a typical “sillén” phase, in which Bi–O layers and (CO_3) layers are intergrown with the plane of the (CO_3) group orthogonal to the plane of the Bi–O layer.²⁹ The Bi–O layer is represented in Fig. 7 projected on (100) and (001), respectively. Within each layer, the Bi1–O and Bi2–O coordination polyhedra are corner-sharing along the (110) and $(\bar{1}\bar{1}0)$ facets (*i.e.*, the $[\bar{1}10]$ and $[110]$ directions). This arrangement reveals that the (001) face is the most densely packed face of the crystal and that the packing densities are the same on (110) and $(\bar{1}\bar{1}0)$ faces. The crystal growth velocity along various planes is

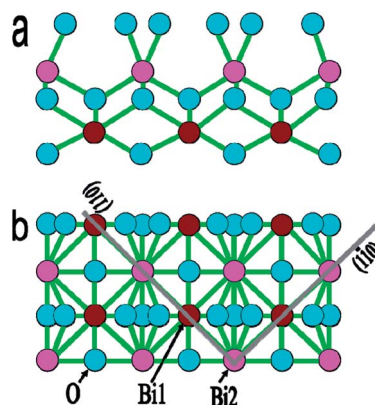


Fig. 7 Schematic representation of the crystal structure of BSC projected on (a) (100) and (b) (001).

dependent upon their atomic packing density. The slowest growth rate is normal to the most densely packed planes. The $\{001\}$ faces would have the slowest growth rate, and hence BSC crystals enclosed by dominant $\{001\}$ faces are commonly observed.^{22,24}

It can be inferred that $[\text{OH}]^-$ ions play dual roles during the growth of the BSC crystals. First, the hydroxide ion is a dominant factor that affects the nucleation and growth behavior of oxide crystals in the hydrothermal synthesis. It has been suggested that $[\text{OH}]^-$ ions adsorb on certain faces of oxide crystals, which may create additional growth anisotropy and modify the growth habit.³⁰ Due to the hindrance effect of $[\text{OH}]^-$ ions on the (110) and $(\bar{1}10)$ facets, the growth rates of these facets are expected to decrease. Therefore, the morphology of BSC crystals gradually changes from irregular shaped plates to square plates. Second, $[\text{OH}]^-$ ions act as the mineralizer in the hydrothermal process; the growth of the BSC crystals should benefit from the increase in the $[\text{OH}]^-$ ion concentration. The $\text{Bi}(\text{NO}_3)_3$ reacts with $[\text{OH}]^-$ ions to form $\text{Bi}(\text{OH})_3$ or $[\text{Bi}(\text{OH})_4]^-$, which are then dehydrated to BiOOH . Meanwhile, the slow hydrolysis of urea is catalysed by $[\text{OH}]^-$ to produce sodium carbonate. As a consequence, the size of BSC crystals increases with increase in the NaOH concentration.

In the hydrothermal synthesis of nanocrystals, foreign ions can act as surfactants to guide the nucleation and growth behaviour of crystals.^{22,31} In our case, the citrate ion plays an important role in the morphogenesis and self-assembly of BSC nanocrystals. As shown in Fig. 7, the $\{100\}$ facets are the most unstable amongst the low-index crystallographic facets of BSC,²⁹ and such facets normally grow rapidly and are suppressed in the final morphology. When citrate ions are present, they will tend to adsorb onto $\{100\}$ faces because their surface energy is much higher than that on the $\{001\}$ and $\{110\}$ facets. The adsorption of citrate ions then blocks further growth on these facets. Consequently, BSC octagonal sheets with new edges enclosed by (100) and (010) facets result. The adsorption of citrate ions on other high-index facets also suppresses their growth rates and leads to the formation of round disks at higher citrate ion concentration. As shown in the TEM and SEM images, the size decreases from nanoplates and octagonal nanosheets, to round nanodisks at the same NaOH concentration, providing evidence of the suppressing effect of citrate ions.

To explore the formation mechanism of 3D BSC nanostructures, the morphologies of 3D BSC nanostructures at different synthesis times were investigated. Fig. 8 shows the SEM images of 3D BSC nanostructures obtained over different synthesis times. BSC nanoplates with sizes of about 100–300 nm and thicknesses of about 20–30 nm can be observed after 30 min. It is interesting to see that these nanoplates are surrounded by sphere-like mud, indicating the growth and self-assembly of nanoplates occurred simultaneously (Fig. 8a and b). After 1 h of reaction, both completed and uncompleted 3D BSC nanostructures with size ranging from about 500 nm to 3 μm were obtained. The morphology of uncompleted nanostructures reveals a layer-by-layer self-assembly formation mechanism (Fig. 8c and d). Well-assembled close-packed 3D BSC nanostructures with size of 3–6 μm were obtained after 6 h of

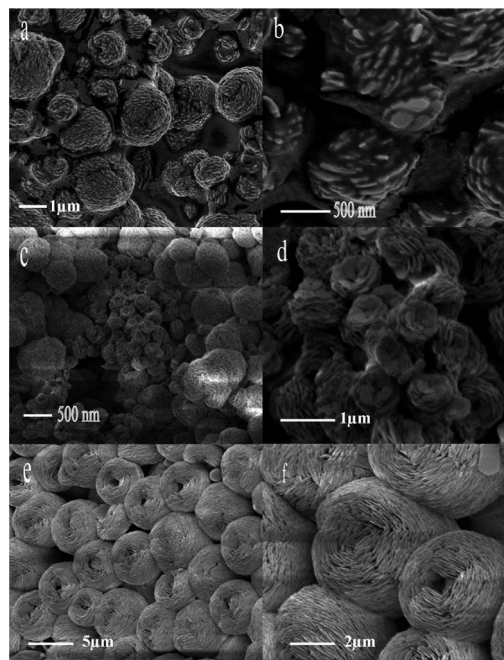


Fig. 8 SEM images of the 3D BSC nanostructures obtained with 30 mmol $\text{Na}_3\text{C}_6\text{H}_5\text{O}_7$ at pH 11 over different synthesis times: (a and b) 30 min. (c and d) 1 h, (e and f) 6 h.

reaction (Fig. 8e and f). It can be inferred that the self-assembly of BSC nanocrystals occurred immediately after the formation of BSC nanocrystals. On the other hand, the plate-like shape of the BSC nanocrystals should also prefer the stack in the $\langle 001 \rangle$ direction. The BSC nanocrystals further grow during the reaction, and both the size and crystallinity increase due to a cementing process by “oriented attachment” on preferred crystal facets after extending the reaction time until the formation of well crystallized, closed packed 3D BSC nanostructures. Fig. 9 shows the SEM images of the 3D BSC nanostructures at different OH^- concentrations. The microstructure of the 3D BSC nanostructures changes due to the morphology of

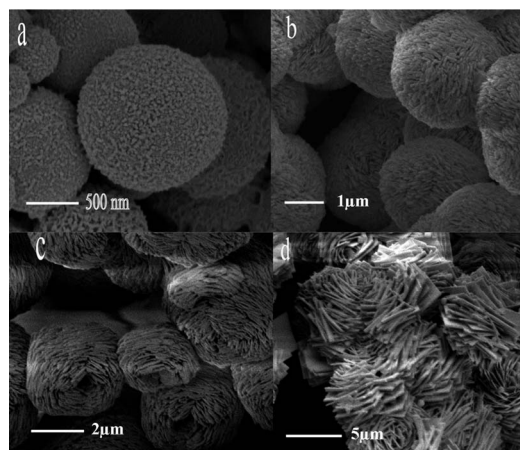


Fig. 9 SEM images of 3D BSC nanostructures obtained with 20 mmol $\text{Na}_3\text{C}_6\text{H}_5\text{O}_7$ at different pH values: (a) 20 mmol $\text{Na}_3\text{C}_6\text{H}_5\text{O}_7$, pH 7. (b) 20 mmol $\text{Na}_3\text{C}_6\text{H}_5\text{O}_7$, pH 10. (c) 30 mmol $\text{Na}_3\text{C}_6\text{H}_5\text{O}_7$, pH 12. (d) 40 mmol $\text{Na}_3\text{C}_6\text{H}_5\text{O}_7$, 2 M NaOH.

BSC nanocrystals changes from nanoparticles to nanoplates with the increase of the OH^- concentration. There is an adsorption competition between OH^- and citrate ions, the increase in OH^- concentration accelerates the growth rate of BSC nanocrystals and also weakens the adsorption of citrate ions. Hence the size of the 3D BSC nanostructures increases markedly with the increase in the OH^- concentration. It is worth noting that citrate ion plays a crucial role in the assembly of nanocrystals. It has been observed that high citrate concentration can produce hexagonal ZnO crystals containing stacked nanoplates.³¹ In our case, citrate ion is the principle reason for the assembly of BSC nanocrystals since the 3D BSC nanostructures can not be obtained in the absence of citrate ions. The adsorption of citrate ions on the $\{001\}$ surface of BSC nanocrystals may balance the interactions among the BSC nanocrystals, binding the BSC nanocrystals into 3D nanostructures. From the above analyses, it can be concluded that citrate and hydroxide ions are the two crucial factors for morphology control of BSC crystals. Their importance depends on their respective concentrations. BSC plates, sheets, or disks occur at lower citrate ion concentration and higher hydroxide concentration, while 3D BSC nanostructures are obtained at higher citrate ion concentration and relatively lower hydroxide concentration. The nucleation, growth and self-assembly of BSC nanocrystals depend on a synergistic effect between the two anions.

The 3D BSC nanostructures were studied for selective adsorption and separation of dyes in order to explore their application for environmental remediation. Two typical dyes, rhodamine B (RhB) and methyl orange (MO), were chosen for investigation. Fig. 10a shows an image of the acidic, neutral, and basic RhB solutions after treatment with 3D BSC nanostructures. It can be seen that the colour of the acidic dye solution faded completely after 20 min. The corresponding remaining concentrations of RhB in acidic, neutral, and basic solutions are plotted in Fig. 10b. Almost 100% of the dye in acidic solution was removed and about 60% is removed in neutral solution, but there is almost no adsorption of the dye in basic solution. The results show that the adsorption of RhB

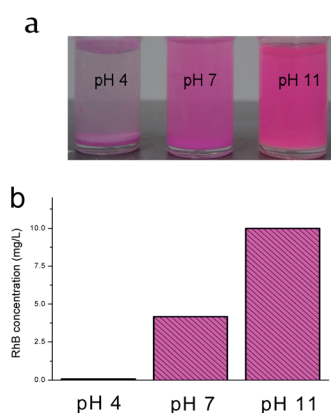


Fig. 10 (a) Image showing the rhodamine B solution and (b) the remaining concentration of rhodamine B after 20 min treatment at different pH.

on the BSC surface strongly depends on the acidity of the solution. The adsorption of RhB on BSC was reversible; the desorption of RhB occurred and the dye solution immediately reverted to a reddish-pink colour when the pH of the solution was adjusted to 11. The 3D BSC nanostructures were then utilized to separate RhB from MO. In order to optimize the separation effect, the experiment was initially carried out under acidic conditions. Fig. 11 shows images of the separation process as it progresses upon addition of the BSC and the corresponding adsorption spectra of the dye solutions. Initially, the solution had an orange-red color reflecting the presence of both dyes. After the addition of BSC, RhB was completely adsorbed by the BSC within 20 min. In contrast, MO remained in the solution and had no obvious adsorption by BSC over the time period. The MO dye was removed first through filtration, and then RhB was released from BSC in distilled water at pH 11. The charging states of the dyes and 3D BSC nanostructure are crucial for the adsorption. The BSC surfaces are negatively charged with a zeta potential of about -40 mV. A dye may adsorb onto its surface by electrostatic and/or van der Waals forces depending on the surface condition. For a negatively charged surface, the attraction of cationic dyes to the BSC surface should be strong through electrostatic forces, while the adsorption of neutral dyes occurs due to van der Waals forces. For anionic dyes, a repulsive force from the BSC surface exists. Adsorption of dye thus results from a balance of repulsion and attraction forces between the surface and the dye molecules. RhB is positively charged, neutral, and negatively charged in the pH range below 6.0, 6.0 to 10.8, and above 10.8, respectively.³² Therefore, RhB adsorption decreases with the increase of pH of the solution. MO, on the other hand, is a negative charged dye;

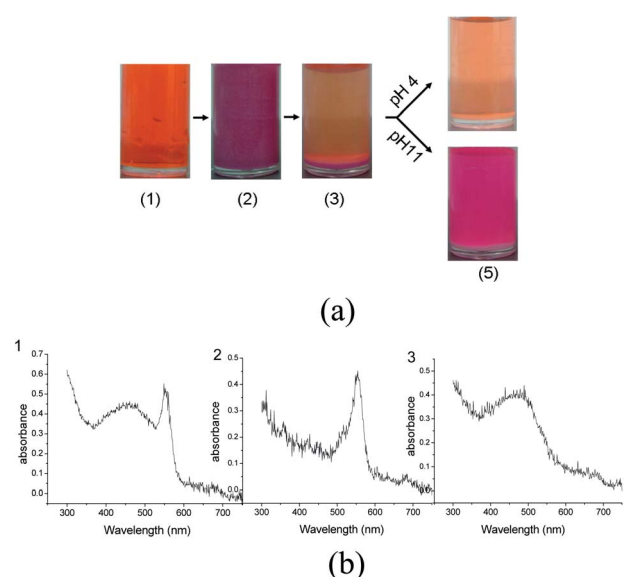


Fig. 11 (a). Separation of MO from a mixture of MO and RhB solution under acidic conditions (pH 4). (1) Prior to the addition of BSC, (2) after addition of BSC for 1 min, (3) after addition of BSC for 20 min, (4) the obtained MO solution, and (5) the obtained RhB solution. (b). Adsorption spectra of mixture of RhB and MO before separation (1), and the obtained RhB (2) and MO (3) after separation.

repulsion between the dye molecule and BSC surface is experienced, and hence no adsorption occurred. We also measured the FT-IR spectra of the 3D BSC samples before and after the adsorption of RhB. As shown in Fig. S2,[†] there was no new band observed, revealing that no chemical bands between RhB and BSC were formed. The adsorbed RhB is easy to be desorbed when the pH changed from 4 to 11. This is also an evidence of electrostatic adsorption. We note that the 3D BSC samples after adsorption of RhB sedimented at the bottom of the bottle and were easily separated from the aqueous solution, thereby constituting a potentially efficient method for charge-selective separation.

Synthesis and characterization of highly sensitive SERS-active substrates is of significant interest for the detection of chemical and biological molecules.^{33–35} Using the preparative technique described here we have developed a new SERS substrate based on a 3D BSC/Au core-shell structure, prepared by depositing a layer of gold nanoparticles (NPs) on the 3D BSC nanostructures. Fig. 12 shows the SEM images of the BSC/Au NP spheres produced. The 3D BSC nanostructures were covered by well dispersed Au NPs of diameters in the range 40–80 nm, and the resulting core-shell spheres retain the shape and size of the 3D BSC nanostructures.

The SERS performance of the 3D BSC/Au NP core-shell spheres was investigated by using benzenethiol as a model analyte. Fig. 13 shows the Raman spectra of benzenethiol adsorbed on three different substrates: 3D BSC nanostructure, a commercial Klarite SERS substrate and the BSC/Au NP core-shell substrates. Raman signals at 417, 691, 999, 1022, 1073, 1110 and 1573 cm^{-1} , originating from benzenethiol,³⁶ were observed for the commercial.

Klarite SERS substrate and the BSC/Au NP core-shell substrates. An excellent correlation between the peak positions and the relative intensities of the two Raman spectra was observed for benzenethiol when adsorbed on the samples. The sensitivity increased remarkably from the commercial Klarite to the BSC/Au NP core-shell sphere substrate. The SERS signal

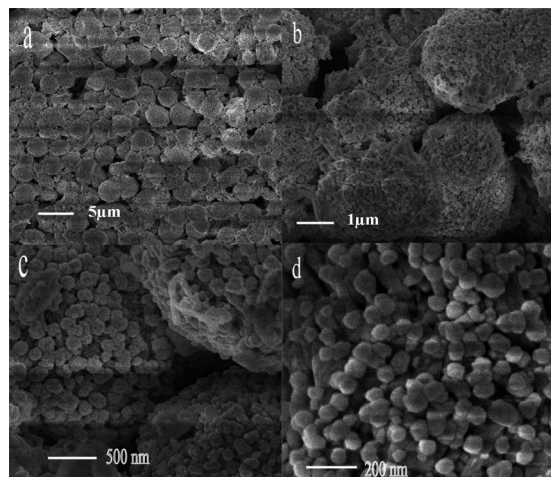


Fig. 12 SEM images of 3D BSC/Au NP spheres at different magnifications.

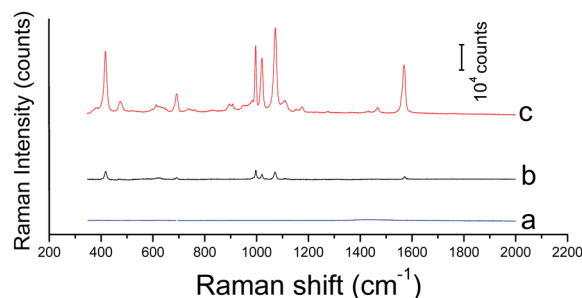


Fig. 13 SERS spectra of benzenethiol adsorbed on (a) 3D BSC nanostructure substrate, (b) Klarite SERS substrate and (c) BSC/Au NP core-shell sphere substrate. The benzenethiol-loading concentration and time are 1 μM .

intensity at 1075 cm^{-1} for the BSC/Au NP core-shell sphere substrate was about 10 times higher than that for the Klarite SERS substrate.

To determine the detection limit of the BSC/Au NP core-shell structures, the SERS substrates were exposed overnight to benzenethiol solutions varying in concentration between 10^{-9} and 10^{-6} M. Fig. 14 shows the SERS spectra of these samples. As expected, the Raman signals of the benzenethiol decrease with decreasing benzenethiol-loading concentration. But the SERS peaks at 999, 1022, and 1110 cm^{-1} can be clearly observed down to a benzenethiol concentration of 1 nM.

It can be inferred that the following three factors mainly contribute to the high SERS intensity for the 3D BSC/Au NP core-shell structures. Firstly, it is well known that the SERS is proportional to the modulus of the localized electromagnetic field squared at the location of the analyte molecule. The interparticle coupling between the gold NPs on the surface of the 3D BSC nanostructures may induce a strong electromagnetic field enhancement, resulting in the high SERS activity.

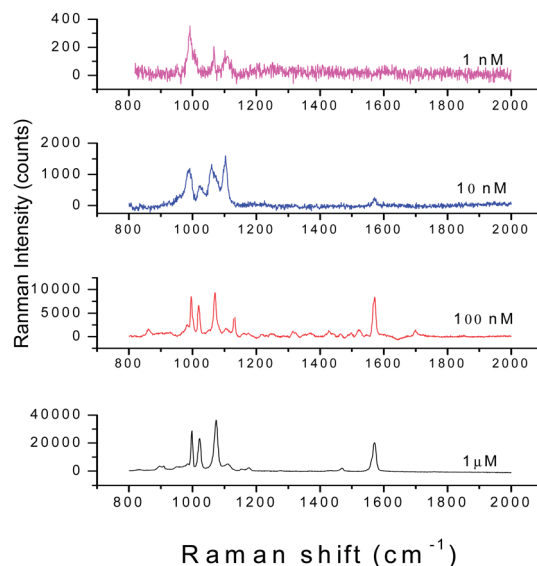


Fig. 14 SERS spectra of benzenethiol adsorbed on BSC/Au NP core-shell spheres as a function of benzenethiol-loading concentration.

Secondly, the 3D spherical feature of the BSC/Au NP core-shell structures preferably scatters more Raman photons into the detector than a flat substrate. Thirdly, the 3D BSC/Au NP core-shell structures tend to adsorb more analytes due to the large number of voids (*i.e.* hot spots) in the structures leading to the high SERS activity. In comparison with the SERS substrates with similar core-shell structures,^{37,38} the BSC/Au NP SERS substrate exhibits competitive sensitivities and shows promise for ultra-sensitive detection of aromatic molecules.

Conclusions

In summary, we present a simple and effective method for morphogenesis and self-assembly of BSC nanocrystals with fully tunable morphologies into 3D nanostructures. The synergistic effect between hydroxide and citrate ions on the formation of BSC nano- and microcrystals and 3D nanostructures has been explored and the formation mechanism has been proposed. The 3D BSC nanostructures have been successfully utilized for selective adsorption and separation of dyes. The SERS substrates based on 3D BSC/gold nanoparticles core-shell spheres exhibit a high sensitivity with detection limit down to 1 nM. The self-assembly of ternary nanocrystals into 3D hierarchical nanostructures may open up new opportunities to fabricate complex and functional superstructures and nanodevices.

Acknowledgements

This work was supported by the Australian Research Council (ARC) (Grant no. DP120104334) and Monash University. This work was performed in part at the Melbourne Centre for Nanofabrication (MCN) in the Victorian Node of the Australian National Fabrication Facility (ANFF). YZ is grateful to UNSW for a Vice-Chancellor's Fellowship. LYY is grateful to the ARC for an Australian Research Fellowship. JRF is grateful to the Melbourne Centre for Nanofabrication for a Senior Tech Fellowship and to RMIT University for a Vice-Chancellor's Senior Research Fellowship. DRM is grateful to the ARC for his Australian Laureate Fellowship.

Notes and references

- S. Mann and G. A. Ozin, *Nature*, 1996, **382**, 313.
- M. Nirmal, B. O. Dabbousi and M. G. Bawendi, *Nature*, 1996, **383**, 802.
- J. Z. Zhang, *Acc. Chem. Res.*, 1997, **30**, 423.
- M. Aguiló and C. F. Woensdregt, *J. Cryst. Growth*, 1984, **69**, 527.
- A. L. Rohl, *Curr. Opin. Solid State Mater. Sci.*, 2003, **7**, 21.
- M. A. El-Sayed, *Acc. Chem. Res.*, 2004, **37**, 326.
- K. P. Stevenson, G. A. Kimmel, Z. Dohnalek, R. S. Smith and B. D. Kay, *Science*, 1999, **283**, 1505.
- Y. G. Sun and Y. N. Xia, *Science*, 2002, **298**, 2176.
- Y. J. Xiong and Y. N. Xia, *Adv. Mater.*, 2007, **19**, 3385.
- B. Lim, T. Y. Yu and Y. N. Xia, *Angew. Chem., Int. Ed.*, 2010, **49**(51), 9819.
- Z. R. Tian, J. A. Voigt, J. Liu, J. McKenzie, B. McDermott, M. J. Rodriguez, M. A. Konishi and H. Xu, *Nat. Mater.*, 2003, **2**, 821.
- F. Li, Y. Ding, P. X. Gao, X. Q. Xin and Z. L. Wang, *Angew. Chem., Int. Ed.*, 2004, **43**(39), 5238.
- M. J. Siegfried and K. S. Choi, *Angew. Chem., Int. Ed.*, 2008, **47**, 368.
- A. Radi, D. Pradhan, Y. K. Sohn and K. T. Leung, *ACS Nano*, 2012, **4**(3), 1553.
- S. H. Yu, H. Colfen, K. Tauer and M. Antonietti, *Nat. Mater.*, 2005, **4**(1), 51.
- K. C. Huang, T. C. Huang and W. F. Hsieh, *Inorg. Chem.*, 2009, **48**(19), 9180.
- Y. N. Xia, Y. J. Xiong, B. Lim and S. E. Skrabalak, *Angew. Chem., Int. Ed.*, 2009, **48**(1), 60.
- K. Miszta, J. D. Graaf, G. Berton, D. Dorfs, R. Brescia, S. Marras, L. Ceseracciu, R. Cingolani, R. V. Roij, M. Dijkstra and L. Manna, *Nat. Mater.*, 2011, **10**, 872.
- Z. P. Zhang, H. P. Sun, X. Q. Shao, D. F. Li, H. D. Yu and M. Y. Han, *Adv. Mater.*, 2005, **17**, 42.
- G. G. Briand and N. Burford, *Chem. Rev.*, 1999, **99**, 2601.
- T. Y. Zhao, J. T. Zai, M. Xu, Q. Zou, Y. Z. Su, K. X. Wang and X. F. Qian, *CrystEngComm*, 2011, **13**, 4010.
- X. F. Cao, L. Zhang, X. T. Chen and Z. L. Xue, *CrystEngComm*, 2011, **13**, 1935.
- F. Dong, W. K. Ho, S. C. Lee, Z. B. Wu, M. Fu, S. C. Zou and Y. Huang, *J. Mater. Chem.*, 2011, **21**, 12428.
- Y. Zhang, F. Duan, M. Q. Chen and Y. Xie, *J. Mol. Catal. A: Chem.*, 2010, **317**(1–2), 34.
- R. Chen, M. H. So, J. Yang, F. Deng, C. M. Che and H. Z. Sun, *Chem. Commun.*, 2006, 2265.
- G. Cheng, H. M. Yang, K. F. Rong, Z. Lu, X. L. Yu and R. Chen, *J. Solid State Chem.*, 2010, **183**, 1878.
- C. Greaves and S. K. Blower, *Mater. Res. Bull.*, 1988, **23**, 1001.
- M. Kellermeier, D. Gebauer, E. Melero-García, M. Drechsler, Y. Talmon, L. Kienle, H. Cölfen, J. M. García-Ruiz and W. Kunz, *Adv. Funct. Mater.*, 2012, **22**(20), 4301.
- J. D. Grice, *Can. Mineral.*, 1999, **37**, 923.
- Y. Chang and H. C. Zeng, *Cryst. Growth Des.*, 2004, **4**, 397.
- Z. R. R. Tian, J. A. Voigt, J. Liu, B. Mckenzie, M. J. McDermott, M. A. Rodriguez, H. Konishi and H. F. Xu, *Nat. Mater.*, 2003, **2**(3), 821.
- Y. J. Oh, T. C. Gamble, D. Leonhardt, C. H. Chung, S. R. J. Brueck, C. F. Ivory, G. P. Lopez, D. N. Petsev and S. M. Han, *Lab Chip*, 2008, **8**, 251.
- G. Braun, I. Pavel, A. R. Morrill, D. S. Seferos, G. C. Bazan, N. O. Reich and M. Moskovits, *J. Am. Chem. Soc.*, 2007, **129**, 7760.
- H. C. Lee, S. B. You, P. V. Pikhitsa, J. H. Kim, S. H. Kwon, C. G. Woo and M. S. Choi, *Nano Lett.*, 2011, **11**, 119.
- G. Q. Liu, W. P. Cai, L. C. Kong, G. T. Duan and F. J. Lu, *J. Mater. Chem.*, 2010, **20**, 767.
- T. H. Joo, M. S. Kim and K. Kim, *J. Raman Spectrosc.*, 1987, **18**, 57.
- C. Yuen and Q. Liu, *Analyst*, 2013, **138**(21), 6494.
- X. Luo, S. M. Lian, L. Q. Wang, S. C. Yang, Z. M. Yang, B. J. Ding and X. P. Song, *CrystEngComm*, 2013, **15**, 2588.